

Local comparison of cup to disc ratio in right and left eyes based on fusion of color fundus images and OCT B-scans

Marzieh Mokhtari^a, Hossein Rabbani^{a,*}, Alireza Mehri-Dehnavi^a, Raheleh Kafieh^a, Mohammad-Reza Akhlaghi^b, Mohsen Pourazizi^b, Leyuan Fang^c

^a Biomedical Engineering Department, School of Advanced Technologies in Medicine, Medical Image & Signal Processing Research Center, Isfahan University of Medical Sciences, Isfahan, Iran

^b Department of Ophthalmology, School of Medicine, Isfahan University of Medical Sciences, Isfahan, Iran

^c Hunan University, College of Electrical and Information Engineering, Changsha, Hunan, China

ARTICLE INFO

Keywords:

Symmetry
Cup to disc ratio
Optical coherence tomography
Color fundus image
Ridgelet transform
Local analysis

ABSTRACT

Symmetry analysis of Optical Coherence Tomography (OCT) images in right and left eyes can lead to introduction of new biomarkers for early detection of eye diseases. In this study, we investigate the symmetry between two eyes by calculating local cup to disc ratio (CDR) from each B-scan based on fusion of fundus images and OCT B-scans. For this purpose, in the first phase, the OCT data of Optic Nerve Head (ONH) in right and left eyes are aligned by finding the equivalent B-scans of both eyes based on the fovea-ONH axes. Since the fovea-ONH axes in OCT data are not available, at first, left and right fundus images are aligned according to their automatically detected fovea-ONH axes. Then, OCT data are registered to corresponding fundus images based on maximum similarity between en-face OCT data and fundus image in each eye. This two-stage alignment procedure depends on 1) the blood vessels, automatically extracted by Hessian analysis of directional curvelet sub-bands, and 2) the disc contour of ONH in fundus images, detected by Distance Regularized Level Set Evolution (DRLSE) algorithm. In the second phase, in order to calculate the local CDRs, the disc and cup boundaries are extracted from the aligned B-scans in left and right eyes. The disc boundary is limited by Bruch-Membrane opening, and the cup boundary is defined by retinal layer border. Therefore, Inner Limiting Membrane (ILM) and Retinal Pigment Epithelium (RPE) layers are extracted using ridgelet transform to find the disc-edge point and cup-edge point in each B-scan. Finally, the ratio of summed areas of cups to summed areas of discs is calculated in corresponding local regions to find the local CDRs. Using this method, we can also introduce a new index called local volumetric CDR (VCDR) by dividing the volume of cup in a specific region to the corresponding volume of disc extracted from OCT images of ONH. Forty healthy OCT datasets of size $650 \times 512 \times 128$ (acquired from Topcon 3D OCT-1000) and corresponding 1536×1612 fundus images were used in this study. In addition to point-by-point comparison of CDRs in equivalent B-scans of aligned OCTs, the CDRs in upper, middle and lower regions were calculated and the maximum symmetry is observed in middle region. In addition, using local VCDR, the symmetry of 3D OCTs of both eyes is analyzed in 24 volumetric sectors.

1. Introduction

To study optic nerve head (ONH) parameters, cross-sectional images (B-scans) from ONH optical coherence tomography (OCT) [1,2] can be investigated. Retinal OCT provides useful information about intra-retinal layers like lamina cribrosa surface, Bruch's Membrane (BM), the border tissue of Elschnig, Retinal Pigment Epithelium (RPE) and its termination within the ONH (Fig. 1). These features in OCT images allow clinicians to identify sclera canal opening or optic disc margin [3,4].

The analysis of symmetry has been used for early detection of eye diseases such as glaucoma [5]. In [6], it has been shown that the cup

and disc sizes of left and right eyes are similar in healthy eyes and in [7] the authors illustrated that Cup-to-Disc Ratios (CDRs) are similar in both eyes of normal subjects. The vertical Optic Disc (OD) diameter and vertical optic CDR were investigated in [8] and the asymmetry analysis on OD parameters in three groups (normal population, people having Ocular Hypertension (OH), and people having Open-Angle Glaucoma (OAG)) were compared. All of these works are based on comparing retinal color fundus images in two eyes. However, symmetry analysis based on other modalities such as OCT, may provide more detailed information. For example, inaccurate disc margin can be extracted by clinicians using fundus images, since BM is invisible and the rim tissue orientation is not considered in fundus images [9]; so, OCT has been used for more accurate evaluation of the disc and cup margin [10]. In addition, OCT can measure the shape of cup more precisely than stereo photographs;

* Corresponding author.

E-mail address: rabbani.h@ieee.org (H. Rabbani).

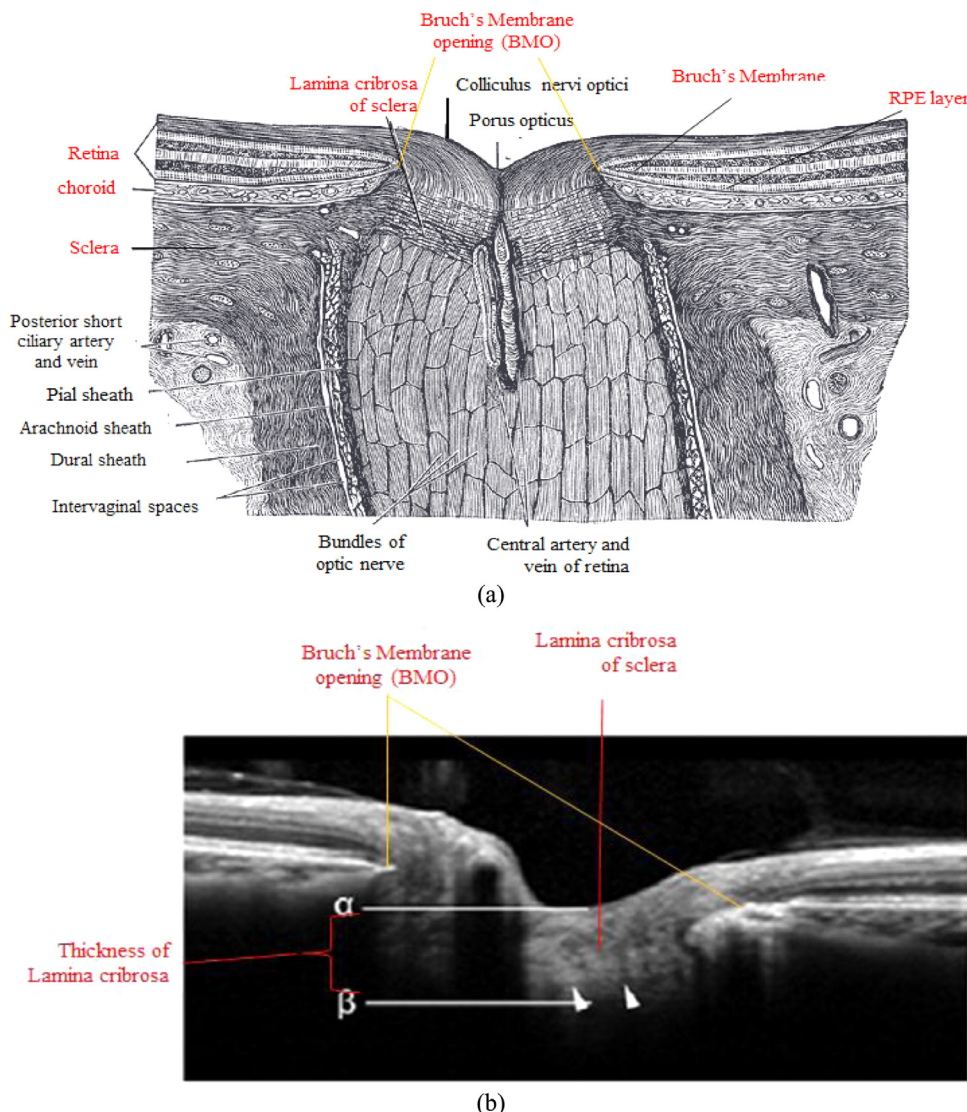


Fig. 1. Anatomical feature can be extracted from OCT data like lamina cribrosa surface, Bruch's Membrane (BM), Retinal Pigment Epithelium (RPE) and its termination within the ONH. (a) Normal histology from ONH, (b) sample OCT B-scan.

especially for some slowly progressive diseases like glaucoma. In this case, three dimensional ONH parameters [11] such as B-scan-based analysis of symmetry can provide appropriate measurements for progression of glaucoma.

To the best of our knowledge, up to now a few studies have been reported for symmetry analysis in OCT images of right and left eyes [12–27]. For example, in [12], the symmetry of macular nerve fiber layer and optic disc measurements in healthy children was investigated. In [13] the symmetry of the Retinal Nerve Fiber Layer Thickness (RNFLT) between the right and left eyes in normal subjects was explored and the most important discrepancy area in RNFL was obtained.

Most of these works perform their comparison without considering any automatic alignments between OCTs [14]. For symmetry analysis, it is important to compare the equivalent parts together to classify the normal against the range of abnormality. The similarity analysis between the same classes would be performed more accurately, if the data acquisition is performed based on the same anatomical positions in OCT data (such as the center of ONH). Even the recent studies which consider the symmetry analysis of OCT data, are only limited on macula and automatic analysis of symmetry around ONH OCT scans has not been reported yet.

Although automatic OCT image analysis has been of a great interest during current years [28–36] only a few works have been dedicated for automatic extraction of cup and disc in B-scans as a complicated job for clinicians to be done quickly and accurately. The only published work in the current years that introduces a multimodal approach to use complementary information in fundus image and OCT data for segmentation of cup and disc margin is reported in [34]. They show that cup boundary and Bruch's Membrane Opening (BMO) ends are easier to detect in OCT data.

In this paper that is an extension of [37], the equivalent B-scans are estimated based on aligning the retinal raphe (i.e., disk-fovea axes) in right and left eyes. Since the retinal raphe is not available in OCT images with small field of view, at first left and right fundus images are aligned using their retinal raphae, then the en-face OCT projections and fundus images of each eye are registered together. The success of this two-step alignment process is mostly dependant on correct estimation of retinal raphae (correct detection of macula and center of ONH). The center of macula is estimated by searching the end points of curvelet-based extracted vessels [38] in Fovea Avascular Zone (FAZ), and Distance Regularized Level Set Evolution (DRLSE) algorithm is used to estimate the center of optic disc in fundus images [39]. After finding equivalent B-scans in right and left eyes, Inner Limiting Membrane (ILM) and Retinal Pigment Epithelium (RPE) layers are detected using ridgelet-based

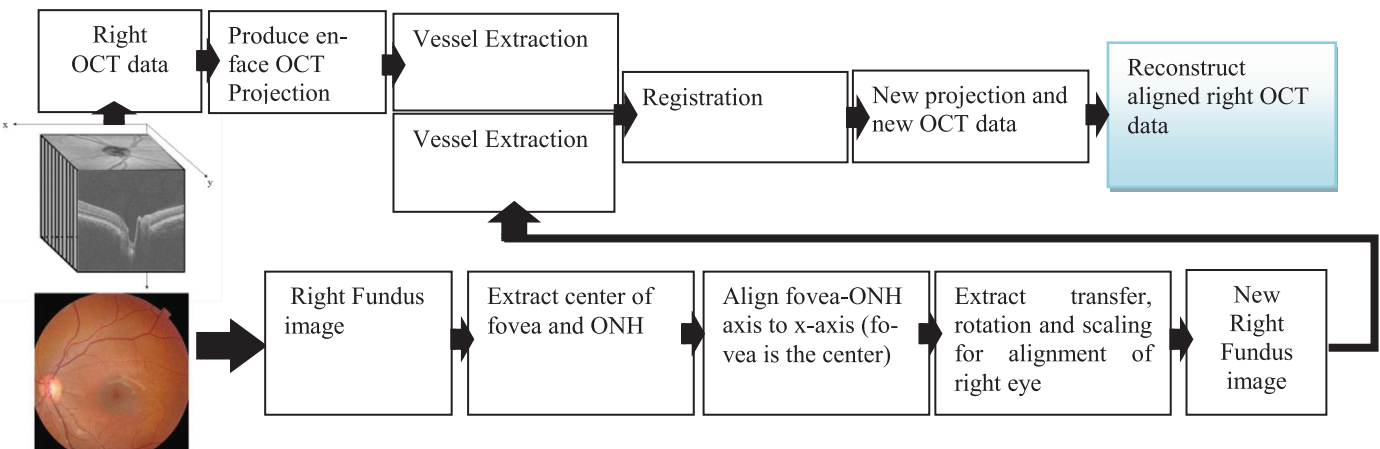


Fig. 2. The proposed algorithm for alignment of OCTs in right eye.

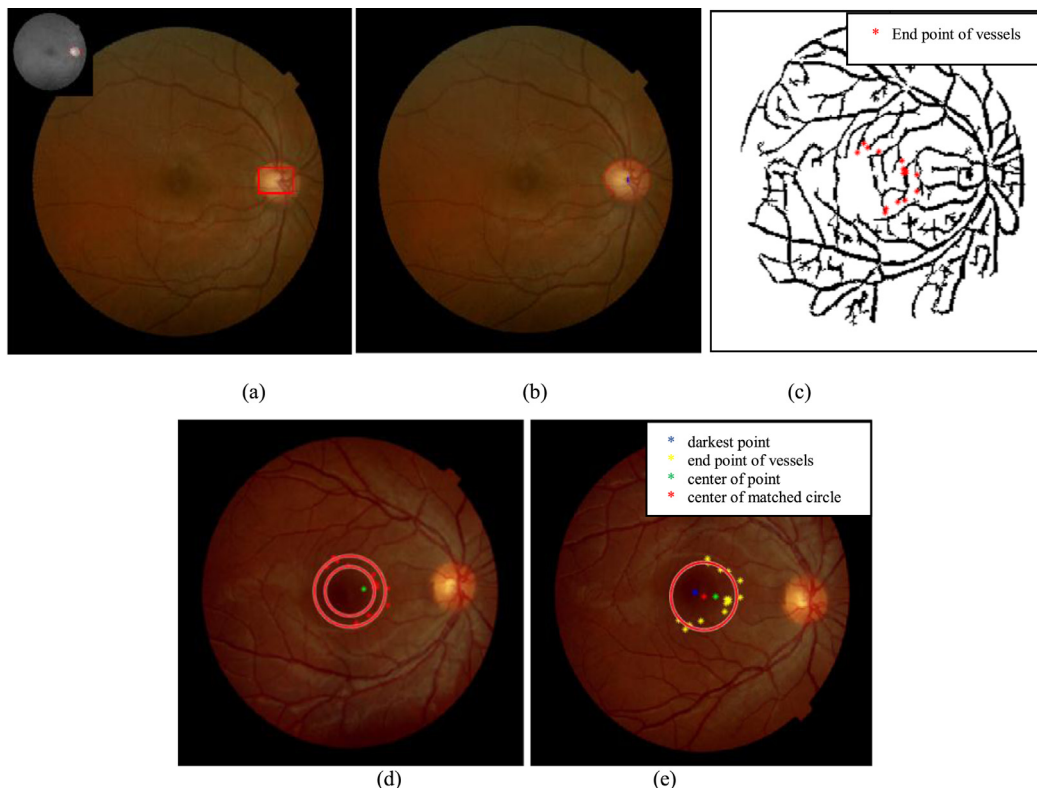


Fig. 3. The results of extraction of center of ONH and macula. (a) the initial contour around the brightest center, (b) the ONH boundary extraction using DRSLE, (c) the end points of vessels in FAZ, (d) two rings with radii 18 and 26 pixels around darkest pixel (the green point), (e) the best matched circle to the selected points between rings (the red point shows the center of this circle that is center of macula). (For interpretation of the references to colour in this figure legend, the reader is referred to the web version of this article.)

methods to extract the disc-edge points and cup-edge points in each B-scan. In this case, a CDR can be extracted from each B-scan and a point-by-point comparison of CDRs in right and left eyes would be provided.

The main contributions of this work are:

1. Introducing a new two-step alignment procedure based on extracted features from macula, ONH and vessels of both color fundus and OCT images for accurate alignment of B-scans of left and right eyes.
2. Employing ridgelet transform for CDR extraction from each B-scan.
3. Local comparison of CDRs in right and left eyes to recognize the best region of symmetry in normal subjects.

4. Introducing a new index called volumetric CDR (VCDR), which is based on a more accurate definition of CDR using volumetric anatomical shape of cup and disc as a new tool for local comparison of CDRs.

The rest of this paper is organized as follows. In [Section 2](#), the proposed method in this paper for alignment of OCT images of right and left eyes is introduced and our ridgelet-based technique for CDR estimation in each B-scan is described. [Section 3](#) reports results of alignments and local comparison of CDRs in right and left eyes of normal subjects. Finally, this paper is concluded in [Section 4](#).

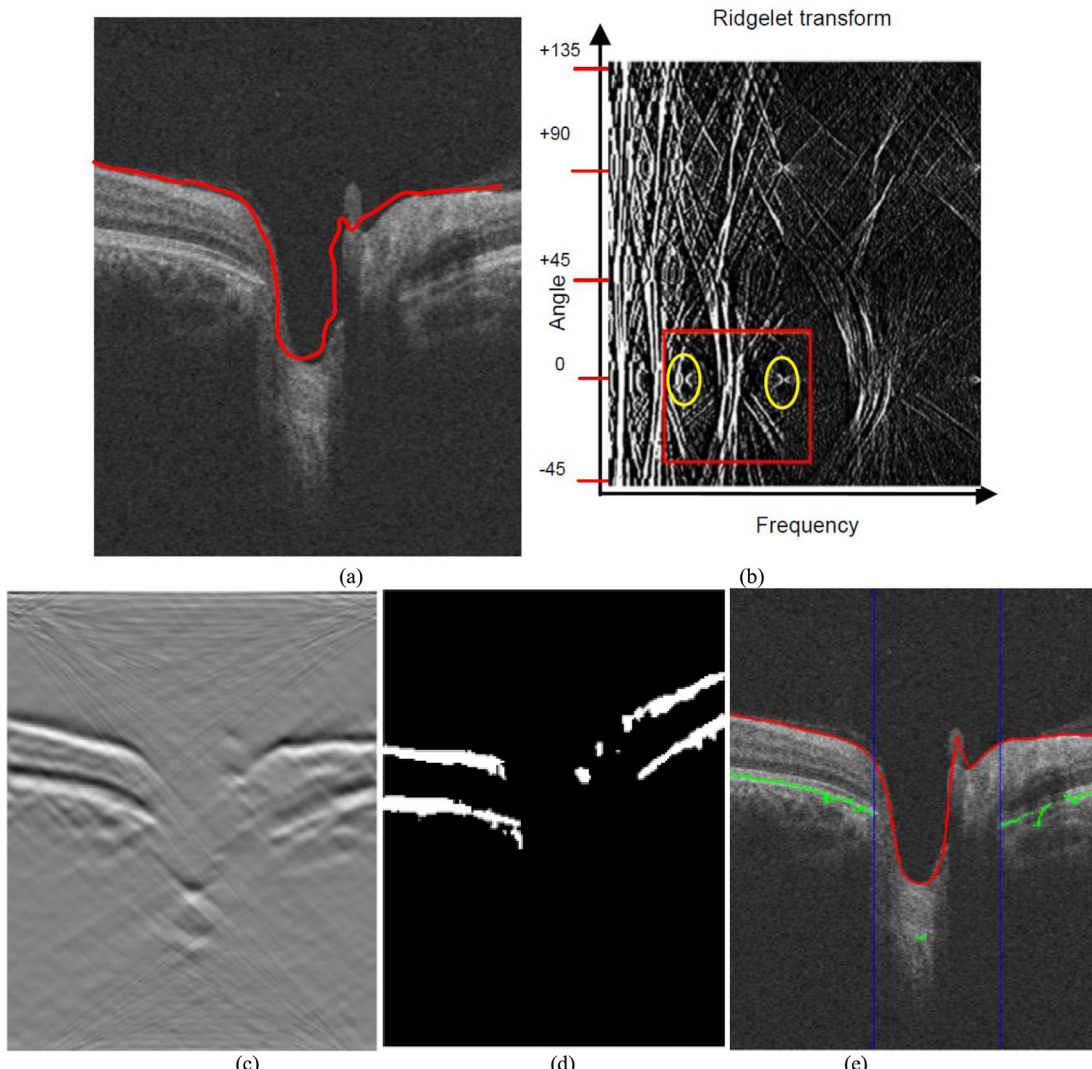


Fig. 4. Main steps for finding the end points of RPE layer. (a) the B-scan image, (b) the coefficient of ridgelet transform and the selected coefficients for image reconstruction, (c) the reconstructed image used for RPE layer segmentation, (d) the binary image after thresholding, (e) the end points of RPE layer (blue lines). (For interpretation of the references to colour in this figure legend, the reader is referred to the web version of this article.)

2. Material and method

2.1. Materials

In this paper, the fundus image and ONH OCT data from both eyes of 40 healthy subjects captured by Topcon 3D OCT-1000 unit (Feyz Eye Hospital, Isfahan) are used for symmetry analysis of local CDRs in right and left eyes. The dimension and resolution of OCT data are $650 \times 512 \times 128$ and $125 \mu\text{m} \times 3.25 \mu\text{m} \times 7 \mu\text{m}$, respectively. The .FDS files of raw data are converted to .MAT file using OCT-EXPLORER software. In addition, the dimension of color fundus images is 1536×1612 in JPEG format. These data is collected from normal subjects with following characteristics:

1. Visual acuity is over 0.6.
2. Power spherical is less than 0.3 diopter.
3. Intra-Ocular Pressure (IOP) is less than 21 mm Hg.
4. The subjects do not have family history of glaucoma and ocular injuries.
5. The CDR is less than 0.6.
6. The subjects are free of ocular and systemic disease that can affect the retinal layers (for example diabetes mellitus).

The data is available online in <https://hrabbani.site123.me/available-datasets/oct-data-color-fundus-images-of-left-right-eyes-of-50-healthy-persons>.

2.2. Estimation of equivalent B-scans in left and right eyes

For comparing the similar areas in two eyes, the OCT data of right and left eyes should be aligned. For this reason, the fovea-ONH axes (retinal raphae) of both eyes are used for registration. Since the field of view in OCT data does not cover both fovea and ONH, we align OCT data of both eyes by the help of their corresponding fundus images. This alignment is composed of two series processes: i.e. 1) alignment of fundus images of both eyes, and 2) registration of fundus images with their corresponding en-face OCT projections (Fig. 2). In [37], the fundus images were registered based on alignment of the retinal raphae to horizontal line. The center of macula and ONH were estimated based on searching the darkest and brightest areas in the middle of fundus images, respectively [37]. In this study as an extended version of [37], the center of macula and ONH are estimated more accurately using the following procedure:

The initial estimate of *center of ONH* is obtained by searching the brightest pixel in fundus image. The estimated center of ONH can be

improved using active contour [30]. For this reason, we use a window around the brightest pixel as initial contour of DRLSE algorithm and segment the ONH boundary. Then the center of ONH is obtained by averaging the position of boundary pixels (Fig. 3a and b).

The *center of macula* is extracted based on the main characteristics of FAZ, i.e. (1) this region is the darkest area in the middle of fundus image, (2) FAZ is a vessel-free area which can be obtained by finding the end points of vessels [40]. In this base, the initial point for the center of macula is found by searching and averaging the darkest pixels in the center of fundus image, and the final point is obtained using the structure of vessels. At first, the initial point is considered as the center of two rings with radii 18 and 26 pixels (the value are obtained empirically. Then, the end-points of curvelet-based extracted vessels [38] between these rings are detected and the center of best circle matched to these points is considered as center of macula (Fig. 3c–e).

After registration of color fundus images of left and right eyes based on alignment of their fovea-ONH axes, the OCT data are registered to their corresponding aligned fundus images. This can be done by first finding the best scaling parameter and then obtaining the optimum amount of rotation based on applying a multi-step correlation-based method [37] on extracted vessels from en-face OCT projection and fundus images. So, the final aligned OCT data of each eye is obtained by applying the registration parameters of en-face OCT projection image to all 2D x-y slices in 3D OCT data (Fig. 2).

2.3. Local comparing of CDRs in right & left eyes

2.3.1. Calculating CDRs in each B-scan

There are different definitions for CDR using OCT B-scan images [41–44]. In this paper, we use the cup and disc boundary definition introduced by Wang et al. [42]. For segmentation of the disc and cup edge points, it is necessary to extract the ILM and RPE layers in B-scans. For this reason, ridgelet transform [45] is utilized to modify B-scan images and ILM and RPE layers are segmented based on A-scan analysis of modified B-scans. The disc boundary is determined as the minimum distance between RPE break points in ONH [46]. These points show BMO and disc margin in projection images [3]. The vertical position of disc edge point is at the end of RPE layer (the blue dash lines in Fig. 6a), and the horizontal position of disc edge point is the position of ILM layer on the selected column (the white points on blue dash lines in Fig. 6a). The cup points are detected on half of the depth of cup at ILM layer (the white points on red dash lines in Fig. 6a), where the cup depth is the distance between disc edge point and the top of the Lamina Cribrosa (the deepest point in ILM layer) [41]. So, it is necessary to detect the RPE breakpoints and ILM layer in B-scan images.

Segmentation of ILM and RPE layers and RPE break points. The ILM layer is the topmost layer in RNFL that is detected by A-scan analysis in each column. At first, the binary image of each B-scan is created by thresholding with an optimum threshold (the threshold value is selected to be 1.4 times of the Otsu threshold). In the binary image, the retinal fiber layer is distinguished from vitreous and the topmost point in each A-scan is detected as boundary of ILM. The speckle noise may create artifacts in segmentation of ILM layer which can be corrected by restricting the distance between neighborhood pixels.

The RPE layer is the brightest amongst retinal layers; so, we can detect it by thresholding the high-intensity pixels of image. However, the extra points near the ONH would distort the segmented RPE layer. Remembering the anatomical structure of RPE, the ridgelet transform is employed to extract edges with near to horizontal direction in ridgelet subbands. The ridgelet transform is a multiscale orientation-selective transform developed to detect the line singularities in natural images [47]. In this work, the coefficients of the ridgelet transform are modified for segmenting the almost horizontally layered structure of retina, which can be approximately proposed as line singularities in specific directions. Comparing to wavelet transform, ridgelets are useful tools to

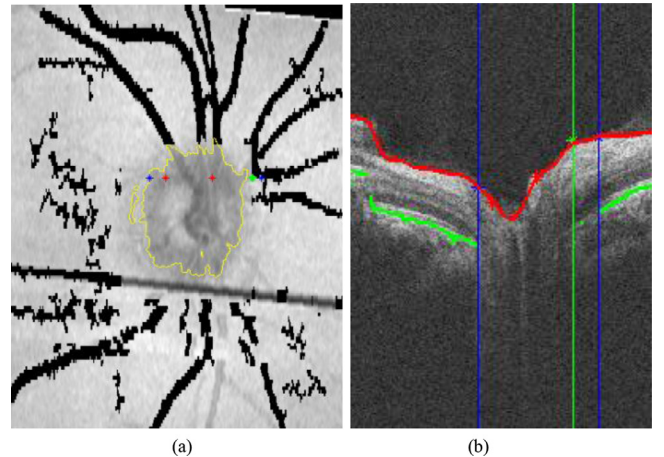


Fig. 5. Improvement of RPE break points. (a) The projection image that the blue points are initial RPE break points, the yellow curve is the disc margin extracted in projection image by active contour and the green point is modified RPE break point in projection image. (b) the corresponding B-scan that the blue and green lines are corresponding to blue and green points in a. (For interpretation of the references to colour in this figure legend, the reader is referred to the web version of this article.)

detect the line and curve structures instead of point singularities. Each ridgelet subband is representing a limited orientation and resolution. For improving the layered structure of retina, the coefficients between -30 to 30° in middle band are selected and other coefficients are set to zero. In the next step, the reconstructed image is constructed by applying inverse ridgelet transform. The image is then thresholded by 1.4 times of Otsu threshold for extraction of RPE layer. In this method, selection of a limited range of orientation for image reconstruction, restricts the discontinuity in the extracted RPE. Finally, the disc margin in each B-scan is detected by selecting the maximum distance between RPE breakpoints in ONH. Fig. 4 shows the result of each step for segmenting RPE layer and finding RPE break points.

The other problem in segmentation of RPE layer is presence of blood vessels near the ONH. The shadow of these vessels may corrupt the end region of RPE near the ONH. To overcome this problem, the following steps are proposed:

- The vessels of en-face OCT projection image are extracted using curvelet transform [38]. The curvelet transform decomposes the input image to multi-directional outputs, so, it can extract the thin and low contrast vessels in each direction [48]. In this method, curvelet sub-bands are extracted and vessel centerlines in each sub-band are segmented using intensity and eigenvalues features. Finally, the vessel of selected sub-bands are combined together and false detected vessels are removed [38].
- The disc margin in projection image is segmented using active counter and the vessels out of disc are selected.
- In the projection image, we select a window around the disc edge point and this window is searched for presence of vessels. If any vessel would be detected, the RPE break point is transferred to the end of vessels in border of disc margin in projection image.

Therefore, the incorrect RPE break points are improved by position of disc margin in projection image. This algorithm shifts the initial end points of RPE layer to the end point of vessels out of the disc (Fig. 5).

Detection of cup and disc edge points in projection image. As mentioned above, the disc edge points are determined with ends of RPE layer and the cup edge points are determined in half of distance between disc edge points and the deepest point in ILM layer. These results are shown in Fig. 6a and these points in each B-scan are transferred to corresponding scan position in the en-face OCT projection image. After finding CDRs

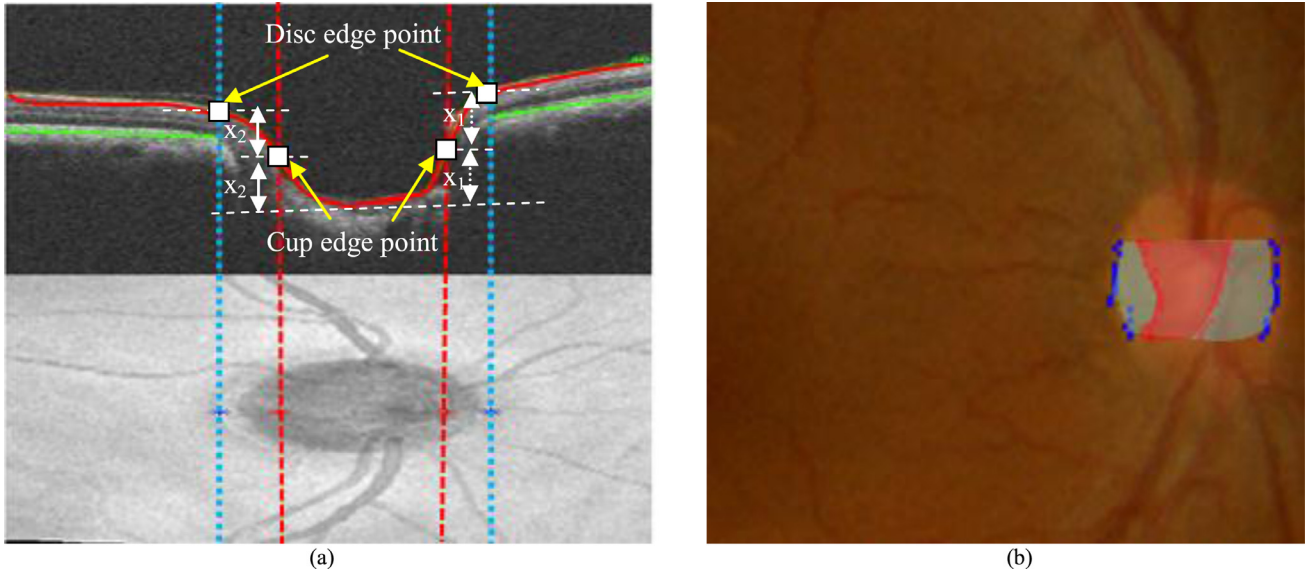


Fig. 6. Extraction of cup and disc margin in each B-scan. (a) Definition of cup and disc in each OCT B-scan and their corresponding points in en-face OCT projection image. (b) Mapping of extracted cup and disc points from B-scans to corresponding fundus image.

in each B-scan, we can evaluate area CDRs in projection image. Similarly, the disc edge points and cup edge points in en-face OCT projection image are transferred to fundus image (after registration of en-face and fundus images) demonstrated in Fig. 6b. As we can see, the area surrounded by disc edge points (blue points) would be the disc area, and the area surrounded by cup edge points (red points) would be the cup area. Therefore, the global CDR is obtained by dividing the cup area to disc area. For analysis of local CDRs, we separate the disc area to three regions, i.e. upper, middle and lower region of disc and the local CDR is obtained in each region.

2.3.2. Volumetric CDRs

In order to have a better approach to evaluate the CDRs we introduce a new definition of CDR based on the volumetric shapes of cup and disc. The corresponding cup area in each B-scan is the surface surrounded between the connecting line of two disc edge points and the ILM layer. Similarly, the corresponding disc area in each B-scan is the surface surrounded between the connecting line of two disc edge points and the lamina sclera border.

In order to have a definition of volumetric cup & disc, at first a short description about anatomical structure of cup and disc is presented (according to Fig. 1). The optic disc is the area in the posterior pole where the ganglion cell axons converge to exit the eye and leave towards the brain. A dense fibrous tissue, the Elsching's ring, defines its margins. The neuroretinal rim that contains the retinal ganglion cells axons covers the disc area and the cup is in the center of disc without retinal cells. The ganglion cells axons leave the eye by pricking the lamina cribrosa (thinned part of the sclera). The axons are arranged in bundles and exit the eye from the tiny holes of the lamina cribrosa to form optic nerves. The size of optic disc and the number of the axons that travel through optic disc make the real size and shape of the cup and rim. The morphological features of the optic disc including disc edge point, ILM layer and RPE-break points (Elsching's ring) and lamina cribrosa should be taken into account in order to estimate the ONH [49].

The lamina sclera border is undetectable in parallel B-scans captured from optic nerve head. So, we restructured radial B-scans to evaluate disc volume. The main steps to calculate the volumetric CDRs are described as below:

2.3.2.1. Radial B-scan extraction¹. Parallel OCT B-scans do not cover the center of optic nerve head needed for detection of lamina cribrosa (appointed around of optic nerve head). So, we extracted the radial B-scans from 3D-OCT data. For this purpose, each radial B-scan in specific direction θ is obtained by axial rotation of 3D-OCT data ($\theta \in [0^\circ, 360^\circ]$) around the center of ONH. Indeed, the central B-scan in each θ -rotated data would be the radial B-scan oriented in $360^\circ - \theta$. If we produce R radial B-scans from each OCT volume, i.e.

$$\theta_i = i \times (\pi/R)^\circ, i = 0, 1, \dots, R - 1. \quad (1)$$

2.3.2.2. Extraction of disc and cup boundary in each radial B-scan. The disc edge point, ILM layer and Elsching's ring are obtained using the proposed method in Section 2.3.1. The lamina cribrosa is dense fibrous under ILM layer that intensity of its pixels in OCT data are different from cup area and vitreous (Fig. 1). The disc area is the surface surrounded to the connecting line of two disc edge points and the lamina sclera border limited to RPE break points (shown with green area in Fig. 7a). The cup area is the surface surrounded between the connecting line of two disc edge points and ILM layer (shown with red area in Fig. 7a). The cup covers center part of disk without neroretinal fibers.

2.3.2.3. Calculating the local volumetric CDR for each sector between two radial B-scans. To estimate the local volume of cup and disc between two radial B-scans, the sector volumes should be approximated (Fig. 7b).

In order to calculate the disc volume of each sector, we add the vertical quasi-rectangular pages from the disc center to RPE break-points as shown in Fig. 7b; i.e.

$$v_{\text{sector}} = \sum_{i=\text{disc_center}}^{\text{RPE_break}} h_{r_i} \cdot r_i \cdot \left(\frac{\pi}{R}\right), \quad (2)$$

where h_{r_i} shows the height of i th vertical page and $r_i \cdot (\frac{\pi}{R})$ is an approximation of its width (the length of each arc with $\frac{\pi}{R}$ angle and r_i radius). For 40 healthy subjects captured by Topcon 3D OCT-1000 unit in this study, we produced 12 radial B-scans from each OCT volume, so, we can compare VCDRs between left and right eyes locally and the symmetry between two eyes in 24 volumetric sectors would be evaluated.

¹ As we can see in Fig. 6b, the complete OD and cup boundaries are not available and the OD boundary is not as typically expected at the bottom sector. By radial capturing of B-scans, these limitations would be resolved and so radial B-scan extraction is only needed when the original OCT data is captured in parallel.

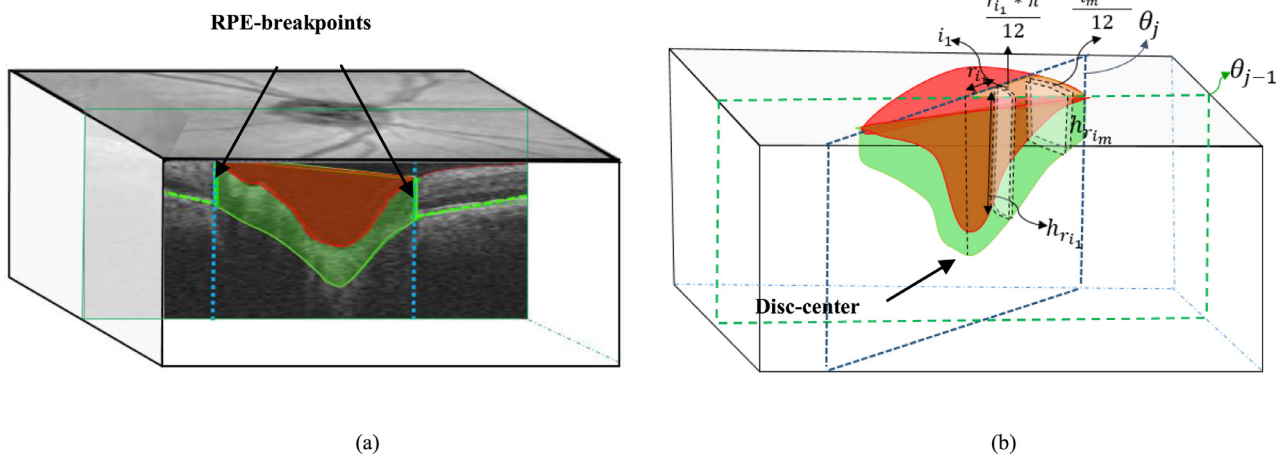


Fig. 7. Calculation of local volumetric CDR (VCDR). (a) A sample radial B-scan of OCT data obtained by axial rotation of 3D OCT data around the center of ONH. The disc area is the surface between line that connect two disk edge points and lamina sclera border (green area). The cup area is the surface between line that connect two disc edge points and ILM layer (red area). (b) The volume of cup and disc and the local volume restricted between two radial B-scans. (For interpretation of the references in this figure legend, the reader is referred to the web version of this article.)

3. Results

3.1. Alignment of B-scans of right and left eyes

The OCT data from ONH of right and left eyes of 40 healthy subjects captured by a Topcon 3D OCT-1000 unit (as described in Section 2.1) are aligned according to proposed method in Fig. 2. Then the point-to-point CDRs are obtained from extracted cup and disc points (area) in corresponding B-scans of left and right OCT data. In order to show the accuracy of our described method in Section 2.3.1, the detected disc margin by our method was compared against manual expert marking for 225 B-scans and an error of 10.25 ± 18.78 pixels (i.e. $32.03 \pm 58.68 \mu\text{m}$) was obtained. Since the mean value of disc margins is 145.07 ± 38.96 , the error of proposed method would be 7% ($\frac{10.25}{145.07} \approx 0.07$).

We can compare the corresponding B-scans before and after alignment visually. Fig. 8 shows two corresponding B-scans before and after alignment. After this alignment, the equivalent B-scans in two eyes are selected based on the fovea-ONH axis. Therefore, the B-scan from the center of the ONH and macula in two eyes are equivalent. We can figure out the similarity between two equivalents B-scans in two eyes by comparing the depths of cup. It shows that the equivalent B-scans have similar cup depths (Fig. 8). Difference between the depth of corresponding B-scans in right and left eyes is evaluated for comparing the similarity between B-scan after alignment. This difference after alignment is 33.792 ± 30.303 pixels (that is less than 15% of cup depth) while it was 156.30 ± 66.24 before the alignment. After alignment, the B-scans are valid enough for comparison of clinical features in both eyes.

3.2. Analysis of point-to-point symmetry and local symmetry of CDRs and VCDRs in left and right eyes

For local analysis of CDRs, the disc area is separated to three regions, i.e. upper, middle and lower regions. The analysis of local symmetry in different regions is useful to find the best region to survey symmetry in normal subjects. The mean and Standard Deviation (SD) of CDRs in left and right OCT data, along with difference between CDRs of left and right eyes are shown in Table 1. This table shows that the difference between CDRs of left and right eyes is less in the middle region, i.e. the most symmetry is observed in the middle region.

The other analysis of symmetry is comparing two signals of CDRs, which each point in these signals corresponds to CDR in a specific part of ONH. As a result, a point-to-point comparison between CDRs of right and

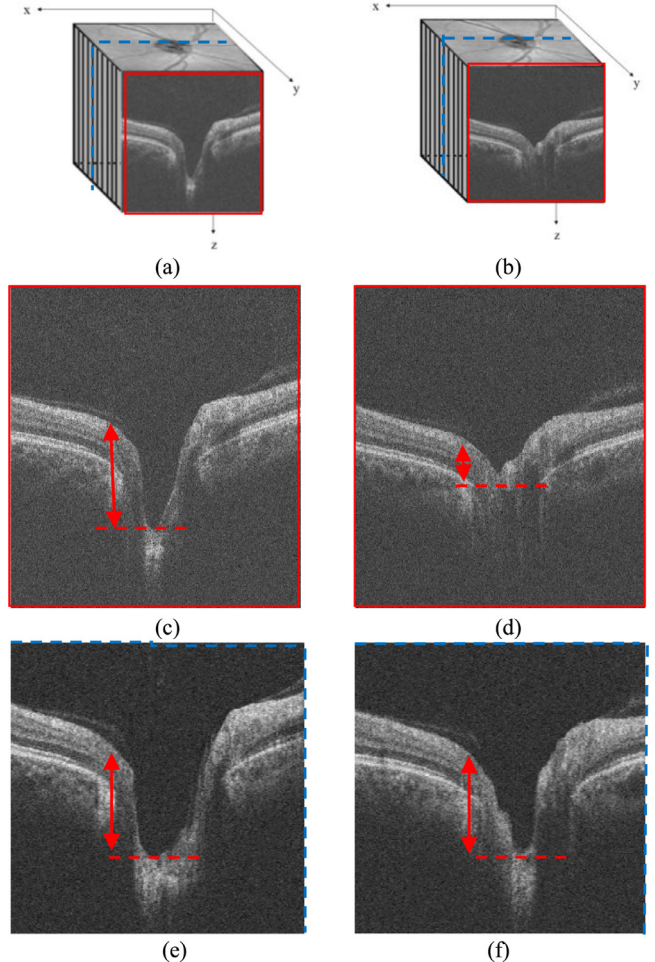


Fig. 8. The comparison of cup depths before and after alignment. (a) and (b) show right and left original OCT data, (c) and (d) show corresponding B-scans in left and right eyes before alignment, (e) and (f) show corresponding B-scans in left and right eyes after alignment. Double Arrow shows that the equivalent B-scans have similar cup depths.

Table 1

Comparison of local CDRs in left and right eyes of 40 healthy subjects.

| CDR | | Mean | STD | MD | SD |
|---------------|------------|------|-------|-------|-------|
| Upper region | Right eyes | 0.43 | 0.055 | 0.049 | 0.043 |
| | Left eyes | 0.44 | 0.064 | | |
| Middle region | Right eyes | 0.43 | 0.061 | 0.042 | 0.039 |
| | Left eyes | 0.44 | 0.074 | | |
| lower region | Right eyes | 0.40 | 0.063 | 0.068 | 0.046 |
| | Left eyes | 0.42 | 0.068 | | |

STD: Standard Deviation.

MD: Mean of Difference between CDR in left and right eyes.

SD: Standard deviation of Difference between CDR in left and right eyes.

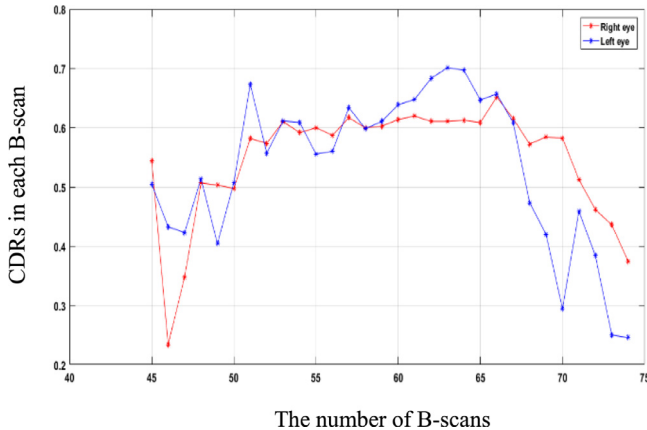


Fig. 9. The cup to disc ratio in left and right eyes of a sample data. Note that the number of B-scans is limited from 45 to 75, because only these B-scans are remained in the common area between two eyes after alignment.

left eyes is provided with potential to lead to a new imaging biomarker for eye disease detection (Fig. 9).

As another comparison strategy, symmetry analysis between two eyes using local VCDRs is performed using the proposed method in

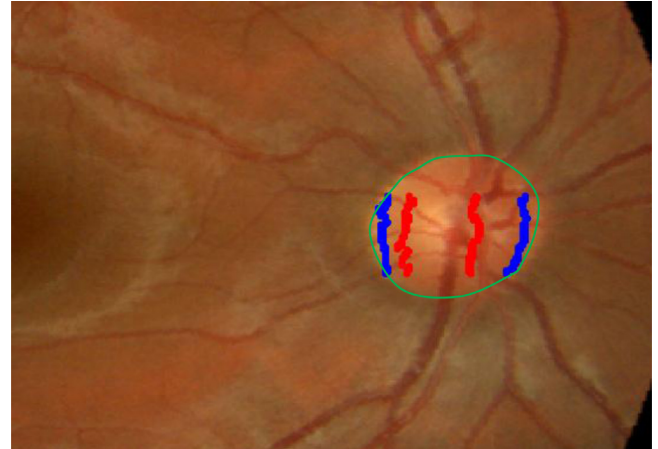


Fig. 11. The difference between disc margin detected based on the end points of RPE in OCT B-scans and the segmented optic disc by changing intensity of color in fundus image. The green curve is disc margin in fundus image extracted by active contour and the blue and red points are respectively the disc and cup margins depicted based on transferring the disc and cup points from OCT B-scans to fundus image. (For interpretation of the references to colour in this figure legend, the reader is referred to the web version of this article.)

Section 2.3.2 (each radial B-scan is segmented to two areas vertically, i.e. 24 sectors are used for local VCDR analysis). Fig. 10 shows the local VCDRs in 24 sectors.

The mean value of local VCDRs in all 24 sectors for 40 data is 0.3249 ± 0.0715 and 0.3344 ± 0.0748 for left and right eyes, respectively. The mean of difference between left and right local VCDRs is 0.0284 ± 0.0184 . The difference between each sector of two eyes are less than 10% of local VCDR, so there are similarity between corresponding sectors of two eyes in normal subjects and this analysis is a good candidate to determine abnormality automatically.

3.3. Extraction of cup and disc margin in fundus image

As we explained before, our method is based on registration of fundus image and OCT data. So, we can transfer the disc and cup edge

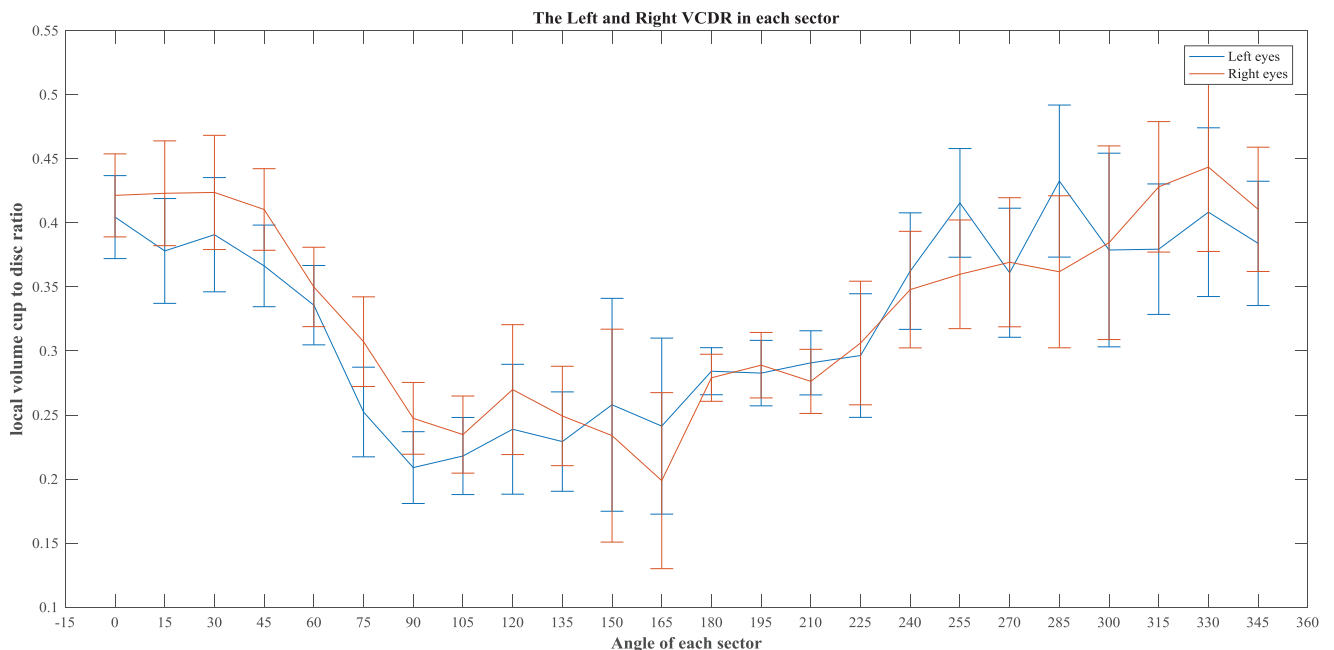


Fig. 10. The local VCDRs in 24 sectors of left and right eyes.

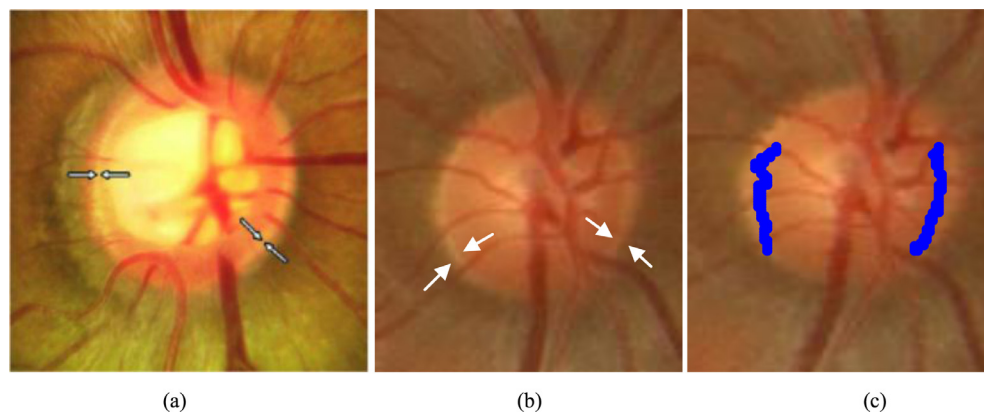


Fig. 12. The similarity between disc margin identified by internal edge of scleral in color fundus images and disc margin extracted based on B-scans. (a) the disc margin identified by internal edge of scleral (white arrows show the inner margins of appearing white rim) [7]. (b) the fundus image and estimated thin rim (white arrows) of sclera in a sample data of our dataset. (c) the disc margin reconstructed based on B-scans in sample data.

Table 2
Comparison of local CDRs in left and right eyes of healthy subjects.

| | | Mean | Std. Deviation | Std. Error Mean |
|----------|-----------|--------|----------------|-----------------|
| Nasal | Left eye | 0.3984 | 0.08602 | 0.03512 |
| | Right eye | 0.5075 | 0.12543 | 0.05121 |
| Superior | Left eye | 0.4446 | 0.09576 | 0.03909 |
| | Right eye | 0.4180 | 0.12847 | 0.05245 |
| Temporal | Left eye | 0.4881 | 0.12939 | 0.05282 |
| | Right eye | 0.3757 | 0.08949 | 0.03653 |
| Inferior | Left eye | 0.4121 | 0.11097 | 0.04530 |
| | Right eye | 0.4120 | 0.09680 | 0.03952 |

points of each B-scan to the fundus image and compare the edge of disc and cup in two modality of data (i.e. color fundus imaging and OCT). In Fig. 11, the disc margin by analysis of OCT is shown with blue points and extracted disc margin from fundus image is shown by green curve (that is segmented by variation in brightness of fundus image). There are some displacement between disc margins in two modalities that this inconsistency is in agreement with results of other recent researches [31,32].

Exact anatomical localization of disc is not possible in fundus images because exact definition is a white rim (internal edge of scleral) which is occasionally visible in fundus images (Fig. 12a and b) [3], however the proposed method is capable of localizing this exact margin using OCT images rather than fundus images as illustrated in Fig. 12c.

3.4. Volumetric local CDR as a new biomarker for glaucoma detection

In order to show the effectiveness of the proposed volumetric local CDR measure as a new biomarker, 7 healthy and 7 glaucoma data captured by Heidelberg Spectralis were used to quantitatively demonstrate the efficacy of the extracted CDRs for diagnosis of ocular diseases such as Glaucoma. Each data contains a 1536×1536 scanning laser ophthalmoscopy (SLO) image and 24 radial 496×768 B-scans.² Tables 2 and 3 respectively show the comparison results of local CDRs in left and right eyes of healthy and glaucoma subjects in 4 sectors: Superior, Inferior, Nasal and Temporal. Accordingly, Tables 4 and 5 show the results of paired samples test of local CDRs in left and right eyes of healthy and glaucoma subjects, respectively. Since the p-values are more than 0.05 in all sectors of healthy subjects (last column of Table 4), we can conclude that there is no significant difference between calculated CDRs in corresponding sectors of left and right eyes of healthy subjects. However, for glaucoma subjects the p-value in temporal section is less than 0.05, which means the symmetry between calculated CDRs in temporal

Table 3
Comparison of local CDRs in left and right eyes of unhealthy subjects.

| | | Mean | Std. Deviation | Std. Error Mean |
|----------|-----------|--------|----------------|-----------------|
| Nasal | Left eye | 0.4967 | 0.12723 | 0.04809 |
| | Right eye | 0.5400 | 0.12200 | 0.04611 |
| Superior | Left eye | 0.4674 | 0.11438 | 0.04323 |
| | Right eye | 0.4930 | 0.12649 | 0.04781 |
| Temporal | Left eye | 0.4819 | 0.11527 | 0.04357 |
| | Right eye | 0.3991 | 0.09552 | 0.03610 |
| Inferior | Left eye | 0.4926 | 0.08317 | 0.03144 |
| | Right eye | 0.5084 | 0.10198 | 0.03855 |

sections of right and left eyes is not valid for glaucoma subjects (i.e. there is a significant differences between temporal CDRs in right and left eyes).

The accuracy of our described method in Section 2.3.2 for VCDR calculation was evaluated by comparing the average error between computed VCDR and ground-truth VCDR in the Superior, Inferior, Nasal and Temporal sectors (Table 6).

In order to show the effectiveness of the proposed volumetric local CDR measure for diagnosis of glaucoma, the paired samples correlations of VCDRs in left and right eyes of healthy and unhealthy subjects (in Superior, Inferior, Nasal and Temporal sections) have been shown in Tables 7 and 8, respectively.

Since the p-value in both healthy and glaucoma subjects in temporal section is less than 0.05, and the correlation between VCDRs between left and right eyes of healthy subjects are greater than glaucoma subjects, we can conclude that local VCDR in temporal section can be used as a biomarker for glaucoma detection. In these tables, the correlation and p-values using ground-truth segmentations are also reported. Since a similar trend is observed for the Superior, Inferior, Nasal and Temporal sectors between the computed and the ground truth VCDRs (i.e., only the temporal sector is important), it can be concluded that the observed trends are anatomical and not caused by errors in the ONH and cup segmentation.

Moreover, in order to show that volumetric local CDR measure is more helpful than the local CDR measure in the detection of diseases such as glaucoma, the paired samples correlations of local CDRs in left and right eyes of healthy and unhealthy subjects (in Superior, Inferior, Nasal and Temporal sections) have been shown in Tables 9 and 10, respectively.

Since the p-values in corresponding sections in these tables are not less than 0.05, we can conclude that correlation of local CDRs between corresponding sections of left and right eyes cannot be used as a criterion for disease classification, while according to Tables 6 and 7 we observed that correlation of VCDRs in temporal section can be used for glaucoma detection.

² The dataset is accessible from <https://hrabbani.site123.me/available-datasets/onh-based-oct-of-7-healthy-and-7-glaucoma-data-captured-by-heidelberg-spectralis>.

Table 4
Paired Samples test of local CDRs in left & right eyes of healthy subjects.

| | | Paired Differences | | | P-value |
|----------|--------------------|--------------------|----------------|-----------------|---------|
| | | Mean | Std. Deviation | Std. Error Mean | |
| Nasal | Left eye–Right eye | −0.10908 | 0.16498 | 0.06735 | .166 |
| Superior | Left eye–Right eye | 0.02659 | 0.08705 | 0.03554 | .488 |
| Temporal | Left eye–Right eye | 0.11240 | 0.12526 | 0.05114 | .079 |
| Inferior | Left eye–Right eye | 0.00010 | 0.09689 | 0.03956 | .998 |

Table 5
Paired Samples test of local CDRs in left and right eyes of unhealthy subjects.

| | | Paired Differences | | | P-value |
|----------|--------------------|--------------------|----------------|-----------------|---------|
| | | Mean | Std. Deviation | Std. Error Mean | |
| Nasal | Left eye–Right eye | −0.04335 | 0.16441 | 0.06214 | .512 |
| Superior | Left eye–Right eye | −0.02554 | 0.12034 | 0.04548 | .595 |
| Temporal | Left eye–Right eye | 0.08274 | 0.07549 | 0.02853 | .027 |
| Inferior | Left eye–Right eye | −0.01588 | 0.14134 | 0.05342 | .776 |

Table 6
Average error between computed VCDRs and Ground-truth VCDRs in the I,S,N,T sectors.

| | Healthy | | Unhealthy | |
|----------|---------------|--------------|------------|--------------|
| | Mean of error | Std of error | Mean error | Std of error |
| Nasal | −0.00539 | 0.061 | −0.017 | 0.020 |
| Superior | 0.00103 | 0.054 | −0.032 | 0.021 |
| Temporal | −0.0109 | 0.045 | −0.023 | 0.032 |
| Inferior | 0.0089 | 0.052 | −0.018 | 0.016 |

Table 7
Paired Samples Correlations of local VCDRs in left and right eyes of healthy subjects.

| | | Computed VCDR | | Ground-truth VCDR | |
|----------|----------------------|---------------|-------------|-------------------|-------------|
| | | Correlation | P-value | Correlation | P-value |
| Nasal | Left eye & Right eye | .673 | .097 | 0.571 | .237 |
| Superior | Left eye & Right eye | 0.901 | .006 | 0.801 | .056 |
| Temporal | Left eye & Right eye | 0.954 | .001 | 0.910 | .012 |
| Inferior | Left eye & Right eye | 0.974 | .000 | 0.926 | .008 |

Table 8
Paired Samples Correlations of local VCDRs in left and right eyes of unhealthy subjects.

| | | Computed VCDR | | Ground-truth VCDR | |
|----------|----------------------|---------------|-------------|-------------------|-------------|
| | | Correlation | P-value | Correlation | P-value |
| Nasal | Left eye & Right eye | 0.619 | .138 | 0.714 | .071 |
| Superior | Left eye & Right eye | 0.614 | .142 | 0.438 | .325 |
| Temporal | Left eye & Right eye | 0.870 | .011 | 0.893 | .007 |
| Inferior | Left eye & Right eye | 0.431 | .334 | 0.411 | .360 |

Table 9
Paired Samples Correlations of local CDRs in left and right eyes of healthy subjects.

| | | Correlation | | P-value |
|----------|----------------------|-------------|---------|-------------|
| | | Correlation | P-value | |
| Nasal | Left eye & Right eye | 0.130 | | .781 |
| Superior | Left eye & Right eye | 0.505 | | .248 |
| Temporal | Left eye & Right eye | 0.759 | | .048 |
| Inferior | Left eye & Right eye | −0.157 | | .737 |

Table 10
Paired Samples Correlations of local CDRs in left and right eyes of unhealthy subjects.

| | | Correlation | | P-value |
|----------|----------------------|-------------|---------|---------|
| | | Correlation | P-value | |
| Nasal | Left eye & Right eye | −0.189 | | .719 |
| Superior | Left eye & Right eye | 0.736 | | .096 |
| Temporal | Left eye & Right eye | 0.391 | | .443 |
| Inferior | Left eye & Right eye | 0.572 | | .235 |

4. Conclusion

CDRs are used for analysis of symmetry in normal subjects. In order to have a more accurate symmetry analysis, the local CDRs can be compared in both eyes of one person. For this purpose, in first step the left and right OCT datasets are aligned by first registration of left and right color fundus images and then registration of en-face OCT projection images by their corresponding color fundus images. Then the equivalent B-scans are estimated in both eyes in same anatomical position (that have same cup depth). In the next step, the cup and disc boundaries in each B-scan of OCT data are extracted based on modification of ridgelet coefficients for segmentation ILM and RPE layers and finding the endpoints of RPE layer (disc margin in each B-scan). After finding the cup and disc points in each B-scan, the similarity index between two eyes can be extracted locally. In this base, we evaluated the local-CDRs in three regions. In addition, we introduced a new biomarker called local volumetric CDR (VCDR) based on volumetric anatomical shape of cup and disc and used it for local comparison of CDRs in 24 corresponding volumetric sectors of 3D OCT data in right and left eyes. This method can be used to extract CDRs in abnormal subjects and to classify normal and abnormal subjects (e.g. for glaucoma subjects) based on symmetry analysis. The global CDR in normal subjects has a wide range (between 0.0–0.9) which depends on disc size (CDRs are low in small optic nerve head and high in large ONH). Furthermore, in individuals with astigmatic myopic less than –8D, global CDRs do not differ significantly between normal and glaucoma persons. This suggests that local analysis of symmetry can be more important to classify normal and glaucoma subjects in presence of other abnormalities.

In this paper, we used the fundus images to provide the required information about macula/fovea and extract the retinal raphe for alignment of B-scans in right & left eyes. However, when the fundus images are not available we may be able to estimate the location of fovea using the vessel map of OCT enface images of ONH (e.g. by parabola fitting [50]).

Acknowledgment

This study has been financially supported by research grant (number 963226) provided by The Elite Research Committee of the NIMAD (National Institute for Medical Research Development), Ministry of Health and Medical Education, I.R. Iran.

References

- [1] Y. Agoumi, G.P. Sharpe, D.M. Hutchison, et al., Laminar and prelaminar tissue displacement during intraocular pressure elevation in glaucoma patients and healthy controls, *Ophthalmology* 118 (1) (2011) 52–59.
- [2] V.J. Srinivasan, D.C. Adler, Y. Chen, et al., Ultrahigh-speed optical coherence tomography for three-dimensional and en face imaging of the retina and optic nerve head, *Invest. Ophthalmol. Vis. Sci.* 49 (11) (2008) 5103–5110.
- [3] A.S.C. Reis, G.P. Sharpe, H. Yang, et al., Optic disc margin anatomy in patients with glaucoma and normal controls with spectral domain optical coherence tomography, *Ophthalmology* 119 (4) (2012) 738–747.
- [4] N.G. Strouthidis, H. Yang, J.F. Reynaud, et al., Comparison of clinical and spectral domain optical coherence tomography optic disc margin anatomy, *Invest. Ophthalmol. Vis. Sci.* 50 (10) (2009) 4709–4718.
- [5] C. Bowd, R.N. Weinreb, J.M. Williams, et al., The retinal nerve fiber layer thickness in ocular hypertensive, normal, and glaucomatous eyes with optical coherence tomography, *Arch. Ophthalmol.* 118 (1) (2000) 22–26.
- [6] M.J. Hawker, S.A. Vernon, G. Ainsworth, et al., Asymmetry in optic disc morphometry as measured by Heidelberg retina tomography in a normal elderly population: the Bridlington Eye Assessment Project, *Invest. Ophthalmol. Vis. Sci.* 46 (11) (2005) 4153–4158.
- [7] R. Ramakrishnan, R. Krishandas, A.L. Robin, M. Khurana, *Diagnosis and Management of Glaucoma*, JP Medical Ltd, 2013.
- [8] L.S. Ong, P. Mitchell, P.R. Healey, R.G. Cumming, Asymmetry in optic disc parameters: the Blue Mountains Eye Study, *Invest. Ophthalmol. Vis. Sci.* 40 (5) (1999) 849–857.
- [9] B.C. Chauhan, C.F. Burgoyne, From clinical examination of the optic disc to clinical assessment of the optic nerve head: a paradigm change, *Am. J. Ophthalmol.* 156 (2) (2013) 218–227.
- [10] K.M. Ramakrishnan R, Chapter-15 back to basics: structural changes in glaucoma and clinical evaluation of the optic nerve head, in: R. Ramakrishnan, K. SR, K. Mona, R. A. L. (Eds.), *Diagnosis & Management of Glaucoma SE* -, Jaypee Brothers Pvt Ltd, 2013.
- [11] K. Lee, M. Niemeijer, M.K. Garvin, Y.H. Kwon, M. Sonka, M.D. Abramoff, Segmentation of the optic disc in 3-D OCT scans of the optic nerve head, *IEEE Trans. Med. Imaging* 29 (1) (2010) 159–168.
- [12] I. Liberek, S. Chaberek, E. Anielska, K. Kowalska, K. Ostrowski, Symmetry of retinal vessel arborisation in normal and amblyopic eyes, *Ophthalmologica* 224 (2) (2009) 96–102.
- [13] H. Yamada, M. Hangai, N. Nakano, et al., Asymmetry analysis of macular inner retinal layers for glaucoma diagnosis, *Am. J. Ophthalmol.* 158 (6) (2014) 1318–1329.
- [14] Y. Chen, N. Kobayashi, K. Kobayashi, Asymmetry in hemifield macular thickness as an indicator of early glaucomatous structural or functional progression, *Acta Ophthalmol.* 90 (s249) (2012) 0.
- [15] M.S. Alluwimi, W.H. Swanson, V.E. Malinovsky, Between-subject variability in asymmetry analysis of macular thickness, *Optom. Vis. Sci. Off. Publ. Am. Acad. Optom.* 91 (5) (2014) 484.
- [16] J.D. Dalglish, Y.M. Tariq, G. Burlutsky, P. Mitchell, Symmetry of retinal parameters measured by spectral-domain OCT in normal young adults, *J. Glaucoma* 24 (1) (2015) 20–24.
- [17] C. Al-Haddad, R. Antonios, H. Tamim, Interocular symmetry in retinal and optic nerve parameters in children as measured by spectral domain optical coherence tomography, *Br. J. Ophthalmol.* 2014 p. bjophthalmol-2013.
- [18] D.J. Salchow, Y.S. Oleynikov, M.F. Chiang, et al., Retinal nerve fiber layer thickness in normal children measured with optical coherence tomography, *Ophthalmology* 113 (5) (2006) 786–791.
- [19] E. Larsson, U. Eriksson, A. Alm, Retinal nerve fibre layer thickness in full-term children assessed with Heidelberg retinal tomography and optical coherence tomography: normal values and interocular asymmetry, *Acta Ophthalmol.* 89 (2) (2011) 151–158.
- [20] D.L. Budenz, Symmetry between the right and left eyes of the normal retinal nerve fiber layer measured with optical coherence tomography (an AOS thesis), *Trans. Am. Ophthalmol. Soc.* 106 (2008) 252.
- [21] J.-C. Mwanza, M.K. Durbin, D.L. Budenz, et al., Interocular symmetry in peripapillary retinal nerve fiber layer thickness measured with the Cirrus HD-OCT in healthy eyes, *Am. J. Ophthalmol.* 151 (3) (2011) 514–521.
- [22] E.A. Essock, M.J. Sinai, R.D. Fechtner, Interocular symmetry in nerve fiber layer thickness of normal eyes as determined by polarimetry, *J. Glaucoma* 8 (2) (1999) 90–98.
- [23] Y. Kurimoto, K. Matsuno, Y. Kaneko, J. Umihira, N. Yoshimura, Asymmetries of the retinal nerve fibre layer thickness in normal eyes, *Br. J. Ophthalmol.* 84 (5) (2000) 469–472.
- [24] S. Asrani, J.A. Rosdahl, R.R. Allingham, Novel software strategy for glaucoma diagnosis: asymmetry analysis of retinal thickness, *Arch. Ophthalmol.* 129 (9) (2011) 1205–1211.
- [25] T. Mahmudi, R. Kafieh, H. Rabbani, M. Akhlagi, in: *Comparison of Macular OCTs in Right and Left Eyes of Normal People*, SPIE Medical Imaging, 2014, p. 90381W. –.
- [26] J.J. Park, D.R. Oh, S.P. Hong, K.W. Lee, Asymmetry analysis of the retinal nerve fiber layer thickness in normal eyes using optical coherence tomography, *Korean J. Ophthalmol.* 19 (4) (2005) 281–287.
- [27] S.C. Huynh, X.Y. Wang, G. Burlutsky, P. Mitchell, Symmetry of optical coherence tomography retinal measurements in young children, *Am. J. Ophthalmol.* 143 (3) (2007) 518–520.
- [28] R. Kafieh, H. Rabbani, I. Selesnick, Three dimensional data-driven multi scale atomic representation of optical coherence tomography, *IEEE Trans. Med. Imaging* 34 (5) (2015) 1042–1062.
- [29] R. Kafieh, H. Rabbani, S. Kermani, A review of algorithms for segmentation of optical coherence tomography from retina, *J. Med. Signals Sens.* 3 (1) (2013) 45–60.
- [30] R. Kafieh, H. Rabbani, M.D. Abramoff, M. Sonka, Intra-retinal layer segmentation of 3D optical coherence tomography using coarse grained diffusion map, *Med. Image Anal.* 17 (8) (2013) 907–928.
- [31] Z. Hu, M. Abramoff, Y. Kwon, et al., Automated segmentation of neural canal opening and optic cup in 3D spectral optical coherence tomography volumes of the optic nerve head, *Invest. Ophthalmol. Vis. Sci.* 51 (11) (2010) 5708–5717.
- [32] Z. Hu, M. Niemeijer, K. Lee, et al., Automated segmentation of the optic disc margin in 3-D optical coherence tomography images using a graph-theoretic approach, *SPIE Med. Imaging* (2009) 72620U–72620U.
- [33] H. Danesh, R. Kafieh, H. Rabbani, F. Hajizadeh, Segmentation of choroidal boundary in enhanced depth imaging OCTs using a multiresolution texture based modeling in graph cuts, *Comput. Math. Methods Med.* 2014 (2014).
- [34] M.S. Miri, M.D. Abràmoff, K. Lee, M. Niemeijer, J.K. Wang, Y.H. Kwon, M.K. Garvin, Multimodal segmentation of optic disc and cup from SD-OCT and color fundus photographs using a machine-learning graph-based approach, *IEEE Trans. mMedical Imaging* 34 (9) (2015) 1854–1866.
- [35] M. Jahromi, R. Kafieh, et al., An automatic algorithm for segmentation of the boundaries of corneal layers in optical coherence tomography images using gaussian mixture model, *J. Med. Signals Sens.* 4 (3) (2014) 171.
- [36] R. Kafieh, H. Rabbani, et al., Curvature correction of retinal OCTs using graph-based geometry detection, *Phys. Med. Biol.* 58 (9) (2013) 2925.
- [37] M. Mokhtari, H. Rabbani, A. Mehri-Dehnavi, Alignment of optic nerve head optical coherence tomography B-scans in right and left eyes, in: *2017 IEEE Int. Conf. on Image Processing (ICIP)*, 2017, pp. 2279–2283.
- [38] A. Soltanipour, S. Sadri, H. Rabbani, et al., Vessel centerlines extraction from fundus fluorescein angiogram based on Hessian analysis of directional curvelet subbands, in: *Proc. 2013 IEEE ICASSP*, 2013, pp. 1070–1074.
- [39] C. Li, C. Xu, C. Gui, M.D. Fox, Distance regularized level set evolution and its application to image segmentation, *IEEE Trans. Image Process.* 19 (12) (2010) 3243–3254.

- [40] S. Hajeb, H. Rabbani, M.R. Akhlaghi, Diabetic retinopathy grading by digital curvelet transform, *Comput. Math. Methods Med.* 2012 (2012).
- [41] P. Hryncak, N. Hutchings, D. Jones, T. Simpson, A comparison of cup-to-disc ratio measurement in normal subjects using optical coherence tomography image analysis of the optic nerve head and stereo fundus biomicroscopy, *Ophthalmic Physiol. Opt.* 24 (6) (2004) 543–550.
- [42] Y. Wang, Q. Chen, S. Lu, Quantitative assessments of cup-to-disk ratios in spectral domain optical coherence tomography images for glaucoma diagnosis, in: 2013 6th Int. Conf. on Biomed. Eng. & Inf., 2013, pp. 160–165.
- [43] J. Xu, H. Ishikawa, G. Wollstein, et al., Automated volumetric evaluation of stereoscopic disc photography, *Opt. Express* 18 (11) (2010) 11347–11359.
- [44] K.L. Boyer, A. Herzog, C. Roberts, Automatic recovery of the optic nervehead geometry in optical coherence tomography, *IEEE Trans. Med. Imaging* 25 (5) (2006) 553–570.
- [45] M. Mokhtary, H. Rabbani, A. Mehri, R Kafieh, Exact localization of breakpoints of retinal pigment epithelium in optical coherence tomography of optic nerve head, in: Proc. 39th Int. Conf. IEEE EMBS, Korea, 2017.
- [46] G.J. Jaffe, J. Caprioli, Optical coherence tomography to detect and manage retinal disease and glaucoma, *Am. J. Ophthalmol.* 137 (1) (2004) 156–169.
- [47] J. Fadili, J.-L. Starck, Curvelets and ridgelets, in: Encyclopedia of Complexity and Systems Science, Springer, 2009, pp. 1718–1738.
- [48] D.L. Donoho, M.R. Duncan, Digital curvelet transform: strategy, implementation, and experiments, in: AeroSense 2000, 2000, pp. 12–30.
- [49] S.S. Hayreh, Structure of the optic nerve, in: Ischemic Optic Neuropathies, Springer, 2011, pp. 7–34.
- [50] Kh.S. Chin, E. Trucco, L. Tan, P.J. Wilson, Automatic fovea location in retinal images using anatomical priors and vessel density, *Pattern Recogn. Lett.* 34 (10) (2013) 1152–1158.